

JGR Solid Earth

RESEARCH ARTICLE

10.1029/2020JB021356

Key Points:

- One-dimensional full-waveform inversion jointly constrains V_S and Q_S structures of lowermost mantle
- Corrections for focusing effects in D'' improve the geophysical interpretation
- Our V_S and Q_S models suggest variations in temperature and in fraction of post-perovskite

Supporting Information:

Supporting Information may be found in the online version of this article.

Correspondence to:

A. F. E. Borgeaud and F. Deschamps,
anselme@earth.sinica.edu.tw;
frederic@earth.sinica.edu.tw

Citation:

Borgeaud, A. F. E., & Deschamps, F. (2021). Seismic attenuation and S-velocity structures in D'' beneath Central America using 1-D full-waveform inversion. *Journal of Geophysical Research: Solid Earth*, 126, e2020JB021356. <https://doi.org/10.1029/2020JB021356>

Received 18 NOV 2020

Accepted 3 JUL 2021

Seismic Attenuation and S-Velocity Structures in D'' Beneath Central America Using 1-D Full-Waveform Inversion

Anselme F. E. Borgeaud¹  and Frédéric Deschamps¹ 

¹Institute of Earth Sciences, Academia Sinica, Taipei, Taiwan

Abstract We use one-dimensional full-waveform inversion to simultaneously infer the S-velocity (V_S) and anelastic (Q_S) structures of the lowermost 480 km of the mantle in 11 contiguous corridors located beneath Northern South America and Central America. Previous studies in this region have reported the presence of slabs at the core-mantle boundary (CMB) and large variations in the depth of the D'' discontinuity, suggesting local temperature variations. We use transverse component waveform data cut around the ScS phase, including the Scd phase due to the D'' discontinuity, from 31 events beneath South America recorded at USArray stations. The minimum period used in this study is 8 s, allowing us to constrain the fine-scale structure of the D'' region and the depth of the D'' discontinuity. We correct the data for the effect of amplitude focusing due to lateral velocity anomalies (i.e., out-of-plane focusing effect) in D'' on the inferred Q_S structure using three-dimensional waveform calculations. We show that, in the explored region, corrections for out-of-plane focusing effects are necessary to obtain Q_S models that have a reasonable interpretation in terms of temperature and fraction of post-perovskite (pPv). Our final models show regions with high V_S , high Q_S , and an elevated D'' discontinuity, surrounding a low-velocity corridor with lower Q_S and a depressed D'' discontinuity that can be explained by local temperature variations. However, differences between temperature perturbations inferred from V_S and Q_S suggest lateral variations in the fraction of pPv.

Plain Language Summary Because the Earth's mantle is not perfectly elastic, seismic waves are slightly attenuated as they travel through it. Attenuation is mostly sensitive to temperature, with larger temperature leading to stronger attenuation, and can be measured from the analysis of seismic waveforms. More specifically, attenuation is parameterized with the quality factor, Q , which is inversely proportional to the attenuation, that is, lower Q indicates stronger attenuation. Together with the velocity of seismic shear waves (V_S), Q provides key information on the deep mantle thermo-chemical structure. Here, we measure radial profiles of V_S and Q in the mantle lowermost 480 km in 11 corridors located beneath Central America, where a subducted slab is believed to be present. Our results show that V_S and Q are overall larger than their average values at these depths, and that the D'' discontinuity, which is believed to be the signature of the phase transition from bridgmanite to post-perovskite (pPv), is elevated. In the central region, however, V_S is slower, attenuation larger, and the D'' discontinuity is deeper than in surrounding corridors, suggesting a higher temperature. A careful examination of our results suggest that this temperature increase is accompanied by a thinning of the pPv lens.

1. Introduction

The origin of the strong velocity anomalies observed in the D'' layer in the lowermost ~400 km of the Earth's mantle is still debated. Array analysis (Durand et al., 2013; Hutko et al., 2006; Thomas et al., 2004; Whittaker et al., 2015), waveform modeling (Kendall & Nangini, 1996; Ko et al., 2017; Sun et al., 2016), and localized tomography (Borgeaud et al., 2017; Hung et al., 2005; Kawai et al., 2007, 2014; Suzuki et al., 2020) studies all have placed important constraints on small-scale S-velocity (V_S) variations in D'' . V_S anomalies contain information on changes in temperature, composition (e.g., iron content), and fraction of post-perovskite (pPv; Murakami et al., 2004; Tsuchiya et al., 2004) in the lowermost mantle, but their interpretation is not unique. Seismic shear attenuation (Q_S) is believed to be mostly sensitive to temperature (Anderson & Giv- en, 1981). Imaging the Q_S structure can thus help resolve the trade-off between temperature, composition, and mineral phase in the lowermost mantle (Deschamps et al., 2019).

Several studies of the lowermost mantle Q_5 structure have been conducted using differential t^* (anelastic delay time) measurements for pair of phases that are mostly sensitive to the lowermost mantle, for example, S-ScS (Durand et al., 2013; Fisher et al., 2003; Ford et al., 2012), or S-ScP (Liu & Grand, 2018). t^* is measured for each observed record using either the slope of the spectral amplitude ratio between the S and ScS (or ScP) phases (Fisher et al., 2003), or by instantaneous frequency matching (Durand et al., 2013; Ford et al., 2012; Liu & Grand, 2018).

A few studies have also used waveform inversion to jointly infer the V_5 and Q_5 structures of the lowermost (Deschamps et al., 2019; Konishi et al., 2017, 2020), and upper (Fuji et al., 2010; Karaoğlu & Romanowicz, 2018a, 2018b) mantle. One advantage of waveform inversion is to explicitly account for the trade-off between the V_5 and Q_5 structures. The presence of large-scale (compared to the seismic wavelength) velocity anomalies produce a lensing effect, usually referred to as the focusing effect, which affects the amplitude of seismic waves. For body waves, ray theory predicts that the focusing effect is proportional to the second derivative of the velocity field (i.e., its curvature) in the direction transverse to the raypath (Woodhouse & Wong, 1986).

For the upper mantle, several previous studies that inferred the Q_5 structure have applied corrections for focusing effect (Romanowicz & Mitchell, 2015). For the lowermost mantle, however, focusing effects are usually not accounted for by studies using differential t^* , although some studies evaluated its effect on differential t^* measurements. Ford et al. (2012) estimated the strength of focusing by velocity anomalies using synthetics computed for three-dimensional (3-D) axisymmetric models (2.5-D). They found that velocity anomalies can produce differential t^* of ~ 0.1 – 0.4 s, which is $\sim 5\%$ – 20% of the absolute value of their observed differential t^* (but with an opposite sign). Liu and Grand (2018) estimated the strength of focusing effects using two-dimensional waveform calculations, and found that focusing can increase their measured differential t^* by 12%. Since Ford et al. (2012) and Liu and Grand (2018) both used two-dimensional (or axisymmetric) models, contributions from out-of-plane velocity anomalies are not accounted for in the estimation of focusing effect. Depending on the region, this contribution may however be significant, and may affect the geophysical interpretation of inferred Q_5 models.

In this study, we use full (iterative) waveform inversion to infer local one-dimensional (1-D) Q_5 and V_5 models for the lowermost 480 km of the mantle beneath northern South America and southern Central America, and we present a method to approximately correct the data for focusing effects due to lateral V_5 variations in D'' using the 3-D waveform calculations package SPEC-FEM3D_GLOBE (Komatitsch et al., 2015, hereafter referred to as “SPEC-FEM3D”). In this region, previous studies have reported strong V_5 anomalies associated with the subduction of the Farallon slab to the core-mantle boundary (CMB; Borgeaud et al., 2017; Hung et al., 2005; Kawai et al., 2014; Kendall & Nangini, 1996), and important variations in the depth of the D'' discontinuity (Hutko et al., 2006; Ko et al., 2017; Thomas et al., 2004; Whittaker et al., 2015), which suggests the presence of small-scale temperature variations. As discussed in previous studies, one of the key features of the region studied is the presence of a low-velocity corridor located roughly beneath Colombia and extending into the Caribbean sea, surrounded by two high-velocity regions (Borgeaud et al., 2017; Ventosa & Romanowicz, 2015).

2. Data

We use transverse component (SH) waveforms from 31 intermediate- and deep-focus earthquakes (source depths between 202.2 and 629.3 km) located beneath South America and recorded at USArray stations and other smaller networks (Table S1). Figure 1a shows the distribution of events, stations, and raypaths. Events are divided in two clusters, labeled “S” and “N”. Figure 1b shows the bouncing points of ScS phases at the CMB for clusters N (top), and S (bottom), respectively, with colors showing ScS-S travel time anomalies with respect to Preliminary Reference Earth Model (PREM; defined as $dt_{ScS-S}^{obs} - dt_{ScS-S}^{PREM}$), corrected for the 3-D mantle structure above the target region using the global V_5 model SEMUCB_WM1 (French & Romanowicz, 2014; Section 3.3). The ScS bouncing points for clusters S and N sample the structure beneath northern South America, and Central America, respectively. We further divide the records in a total of 11 corridors, labeled N0 to N5 and S0 to S4, with azimuth separations of $\sim 6^\circ$. This corresponds to a spacing of ~ 180 km at the bouncing points at the CMB. The location of corridors are chosen based on the observed

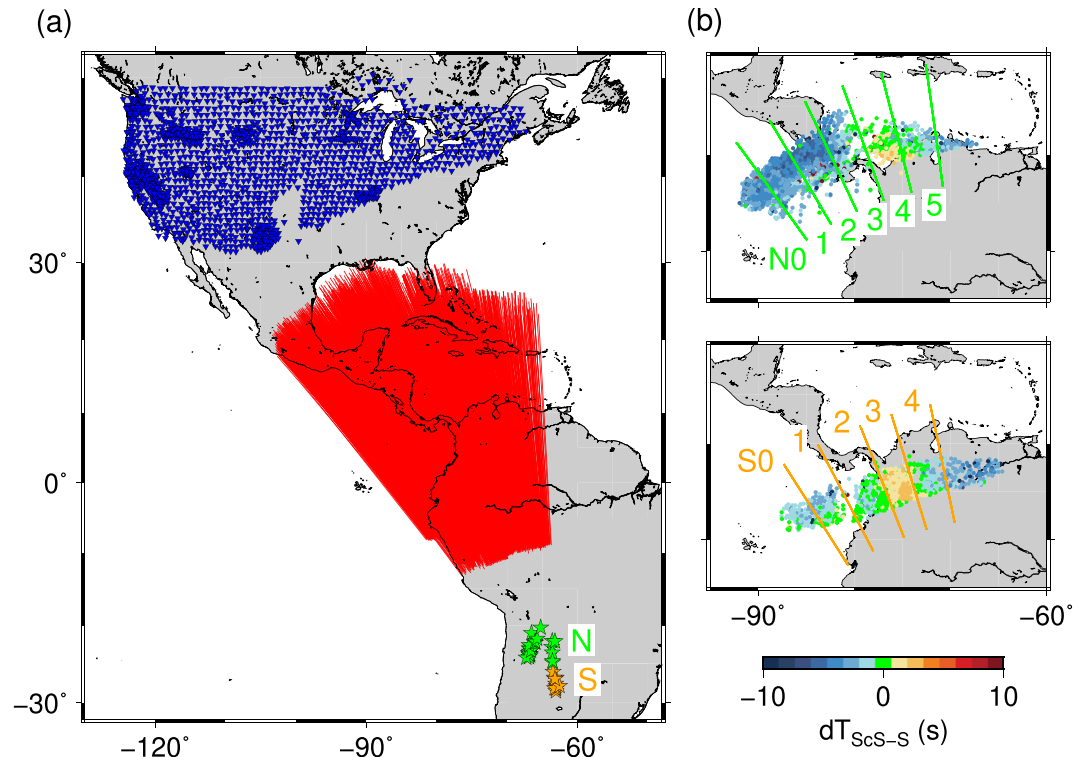


Figure 1. Target region and data set for this study. (a) Events (green and orange stars), stations (blue inverted triangles), and raypaths in the lowermost 500 km of the mantle (red lines) for the data set used in this study. The events are divided in two clusters, labeled N (North cluster), and S (South cluster). (b) Bouncing points of ScS waves at the core-mantle boundary for event clusters N (top panel) and S (bottom panel), with colors indicating ScS-S travel time anomalies with respect to PREM and corrected for the three-dimensional mantle. N0–N5 and S0–S4 denote the 11 corridors in which we invert V_S and Q_S models.

ScS-S differential travel times. In particular, corridor S3 and N4 encompass low (in average) V_S regions reported in, for example, Borgeaud et al. (2017) and Ventosa and Romanowicz (2015). We note that the travel times in Figure 1 are used only to define the corridors (and not in the inversion), and come with possibly large uncertainties. The average differential travel times after correction are given by (N0, N1, N2, N3, N4, and N5) = (2.71, 3.22, 3.24, 2.12, -0.43, and 1.84) and (S0, S1, S2, S3, and S4) = (0.96, 0.75, 0.42, -1.08, and 0.62). In comparison, the travel times before corrections are given by (N0, N1, N2, N3, N4, and N5) = (2.45, 1.85, 1.66, 0.86, -3.47, and -1.40) and (S0, S1, S2, S3, and S4) = (-0.01, -0.88, -0.33, -1.88, and -0.34).

In order to constrain the V_S and Q_S structures of the lowermost 480 km of the mantle, we use waveforms cut around the ScS phase for epicentral distances in the range 70° – 79° . The starting time for each time window is defined as $t_0 = \max(t_{ScS} - 30, t_S + \tau)$, where t_{ScS} , and t_S are the arrival time of the ScS, and S phases (in seconds) computed using TauP (Crotwell et al., 1999) for PREM, and τ is the dominant period of the S wave. The ending time is $t_1 = t_{ScS} + 40$ s. Each record thus includes ScS pre- and post-cursors due to interaction with the D'' discontinuity, in particular the S_{cd} phase, which constrains the depth of the D'' discontinuity. The data are filtered between 8, 12.5, or 20 and 200 s, depending on the corridor and on the iteration number during the iterative inversion. The minimum period for the first iteration is: 20 s for corridors with the largest ScS-S differential travel times (N0–3 and N5); 12.5 s for corridors S0–2 and S4; and 8 s for corridors S3 and N4, which have travel time perturbations small enough to directly use 8 s waveforms. The minimum period for the last iteration is 8 s for all corridors. The small minimum period allows to constrain the detailed radial structure of the D'' layer, and the depth of the D'' discontinuity. As in Konishi et al. (2017), the direct S wave is not used in the inversion, but as a reference phase to correct ScS travel times for the 3-D structure near the source and receivers (Section 3.3). The S phase is, however, not used to correct ScS amplitudes because of significant amplitude anomalies for our data set due to the presence of the Farallon slab in the

mid-mantle (see Text S1 and Figure S1). The waveforms for all time windows are re-sampled to 4 Hz, and assembled into a waveform residual vector $\delta\mathbf{d}_A$ defined as

$$(\delta\mathbf{d}_A[\mathbf{m}])_i = \mathbf{u}(t_i) - \mathbf{s}[\mathbf{m}](t_i), \quad (1)$$

where $\mathbf{s}[\mathbf{m}]$ are the synthetics for the initial model \mathbf{m} (updated at each iteration), \mathbf{u} are the data, and t_i are the time points within each time window.

2.1. Spectral Amplitude Ratio

The waveform misfit associated with the residual vector $\delta\mathbf{d}_A$ is mostly sensitive to differences in travel time. In order to more explicitly account for differences in amplitude between data and synthetics, we also use the logarithmic spectral amplitude ratio, defined as

$$(\delta\mathbf{d}_B[\mathbf{m}])_i = \ln|\tilde{\mathbf{u}}(\omega_i)| - \ln|\tilde{\mathbf{s}}[\mathbf{m}](\omega_i), \quad (2)$$

where $\tilde{\mathbf{s}}$, and $\tilde{\mathbf{u}}$ are the Fourier transforms of the synthetics, and data. Karaoğlu and Romanowicz (2018a) reported that when inverting for the Q_S structure, the spectral amplitude misfit is more robust than the waveform misfit with respect to errors in the velocity model, since it excludes the phase information.

To compute $\delta\mathbf{d}_B$, we use the same time windows as for $\delta\mathbf{d}_A$, apply a taper to each time window, compute the Fourier transform (using FFT), and keep only the amplitude spectrum. We use the part of the spectrum between 7.1 and 25 s, with frequency increments given by $0.125T^{-1}$, where T is the length of each time windows.

2.2. Computation of Synthetics and Data Selection

Synthetics are computed using the direct solution method (DSM; Kawai et al., 2006) down to 3.2 s. We use the Global Centroid Moment Tensor (GCMT) catalog (Ekström et al., 2012) for the centroid time and location and moment tensor components, but we redetermine the source time functions and an amplitude correction for each event in our data set (see Text S2). In agreement with Yamaya et al. (2018), we find that source time function durations in the GCMT catalog for our events are generally overestimated. The event amplitude corrections act as average corrections for the amplitude of the ScS waves to account for the regional average 1-D structure of the upper and mid-lower mantle beneath Central and North America.

The initial model for all corridors is PREM (Dziewonski & Anderson, 1981), except for Q_S in the crust ($Q_S = 300$), and in the upper mantle ($Q_S = 165$). For these regions, Q_S is taken from the initial model of Karaoğlu and Romanowicz (2018a). This Q_S structure is less attenuative than PREM, and represents the high- Q_S region for the shallow 300 km beneath most of the US. Indeed, synthetics computed using PREM Q_S (filtered between 8 and 200 s) have broader S-wave pulses than the data (even using the shorter-duration redetermined source time functions), suggesting that PREM average upper mantle Q_S is too small beneath the US.

We discard abnormal data, and data that differ significantly from PREM synthetics and could lead the inversion toward a local minimum, using the following criteria: (a) zero-lag cross-correlation ≥ 0 ; (b) $0.4 \leq$ amplitude ratio ≤ 2.5 ; and (c) variance ≤ 2.5 , with the variance being defined as

$$\text{variance} = \frac{|\mathbf{u} - \mathbf{s}|^2}{|\mathbf{u}|^2}. \quad (3)$$

For the spectral amplitude ratios data, we further require that the signal-to-noise ratio be greater than four. The reason is that the noise does not cancel out for a large number of spectral amplitude records because of the absolute value in Equation 2, while it approximately does for waveform records. For the final iterations, the number of waveforms per corridor varies between 135 and 759, except for corridor N5, which has only 66 waveforms. The total number of waveforms after selection is 3,729.

3. Method

The method used in this study is based on Fuji et al. (2010) and Konishi et al. (2017), with the following modifications and technical improvements: (a) we added the spectral amplitude misfit to better constrain the Q_S structure, and performed iterative inversion; (b) we used travel time corrections for the 3-D mantle structure above our target region based on global tomographic models; and (c) we applied corrections for focusing effects due to lateral V_S variations in D'' . Due to the presence of strong 3-D anomalies in D'' beneath Central America, which makes it difficult to use linearized 3-D waveform inversion (e.g., Konishi et al., 2020), we used 1-D full (iterative) waveform inversion to jointly infer the V_S and Q_S structures.

3.1. Inverse Problem and Model Parametrization

We invert for the 1-D V_S and Q_S structures of the lowermost 480 km of the mantle (depth range 2,411–2,891 km). Our models are parametrized using 12 layers of 40 km thickness, with constant V_S and Q_S within each layer, resulting in a total of 24 parameters. The inversion consists in finding the V_S and Q_S models \mathbf{m}^k , where $k \geq 1$ is the iteration number, that minimizes the multi-objective function

$$\phi(\mathbf{m}^k) = \frac{1}{|\mathbf{u}|^2} \left(\phi_A(\mathbf{m}^k) + \beta \phi_B(\mathbf{m}^k) \right), \quad (4)$$

where $1/|\mathbf{u}|^2$ is a normalization factor, $\beta \geq 0$ controls the relative importance of the two objective functions (see Text S3),

$$\begin{aligned} \phi_A(\mathbf{m}^k) &= \sum_n (w_A^n)^2 \int_{t_0^n}^{t_1^n} dt |s(t) - \mathbf{u}(t)|^2 \\ &\approx \Delta t \left| \mathbf{W}_A \left(\mathbf{A}^{k-1} \delta \mathbf{m}^k - \delta \mathbf{d}_A^{k-1} \right) \right|^2, \end{aligned} \quad (5)$$

is the waveform misfit, with $\delta \mathbf{d}_A^{k-1} \equiv \delta \mathbf{d}_A[\mathbf{m}^{k-1}]$ defined in Equation 1,

$$\begin{aligned} \phi_B(\mathbf{m}^k) &= \sum_n (w_B^n)^2 \int_{\omega_0}^{\omega_1} d\omega \left| \ln |\tilde{s}(\omega)| - \ln |\tilde{\mathbf{u}}(\omega)| \right|^2 \\ &\approx \Delta \omega \left| \mathbf{W}_B \left(\mathbf{B}^{k-1} \delta \mathbf{m}^k - \delta \mathbf{d}_B^{k-1} \right) \right|^2, \end{aligned} \quad (6)$$

is the spectral amplitude misfit, with $\delta \mathbf{d}_B^{k-1} \equiv \delta \mathbf{d}_B[\mathbf{m}^{k-1}]$ defined in Equation 2,

$$\delta m_j^k = m_j^k - m_j^{k-1} = \delta \ln v_s(r_j) \quad (j = 1, \dots, 12), \quad (7)$$

is the perturbation to model \mathbf{m}^{k-1} for all but the final iteration, and

$$\delta m_j^{\text{final}} = m_j^{\text{final}} - m_j^{\text{final}-1} = \begin{cases} \delta \ln v_s(r_j) & j = 1, \dots, 12 \\ \delta Q_S^{-1}(r_{j-12}) & j = 13, \dots, 24, \end{cases} \quad (8)$$

is the model perturbation for the final iteration. Including Q_S at a stage where V_S is far from the optimal structure results in non-physical Q_S structures, so that we include this parameter in the final iteration only. \mathbf{W}_A and \mathbf{W}_B are the (diagonal) data weighting matrices for the waveform, and spectral amplitude residual vectors. They are defined by $(W_A)_i = (\max |\mathbf{u}|)^{-1}$, and $(W_B)_i = 2(\max \ln |\tilde{\mathbf{u}}| - \min \ln |\tilde{\mathbf{u}}|)^{-1}$, where \mathbf{u} is for the time window that contains time-point t_i .

The partial derivative kernels \mathbf{A}^k and \mathbf{B}^k in Equations 5 and 6 are defined as:

$$A_{ij}^k = \frac{\partial s[\mathbf{m}^k](t_i)}{\partial m_j}, \quad (9)$$

which is the partial derivative of the synthetics s at time-point t_i with respect to model parameter m_j , and

$$B_{ij}^k = \frac{\partial \ln |\tilde{s}[\mathbf{m}^k]|(\omega_i)}{\partial m_j}, \quad (10)$$

which is the partial derivative of the logarithm of the spectral amplitude of the synthetics at frequency point ω_i with respect to model parameter m_j . The normal equation, which defines the inverse problem, is obtained by setting the gradient of the misfit in Equation 4 with respect to $\delta\mathbf{m}$ to zero, implying

$$\left(\mathbf{A}^T\mathbf{W}_A\mathbf{A} + \beta\mathbf{B}^T\mathbf{W}_B\mathbf{B} + \mathbf{\Gamma} + \mathbf{\Lambda}\right)\delta\mathbf{m} = \mathbf{A}^T\mathbf{W}_A\delta\mathbf{d}_A + \beta\mathbf{B}^T\mathbf{W}_B\delta\mathbf{d}_B, \quad (11)$$

where the iteration number k has been omitted for simplicity. $\mathbf{\Lambda}$ is built from the second derivative operator \mathbf{D} and adds smoothness regularization,

$$\mathbf{\Lambda} = \alpha \begin{bmatrix} \lambda_v \mathbf{D}^T \mathbf{D} & \\ & \lambda_q \mathbf{D}^T \mathbf{D} \end{bmatrix}, \quad (12)$$

and $\mathbf{\Gamma}$ is a damping regularization term,

$$\mathbf{\Gamma} = \alpha \begin{bmatrix} \gamma_v \mathbf{I} & \\ & \gamma_q \mathbf{I} \end{bmatrix}, \quad (13)$$

where α is a constant normalization factor so that $\mathbf{\Gamma}$ and $\mathbf{\Lambda}$ have values comparable to the partial derivative kernels when $\lambda_v = \lambda_q = \gamma_v = \gamma_q = 1$ (see Text S3). The parameters λ_v , λ_q , γ_v , and γ_q control the strength of the regularization, with values ranging from 0.01 to 2.4 (Section 5.3). The inversion is conducted iteratively, and the number of iterations varies from $k = 1$ to 3, depending on the corridor.

3.2. Computation of Partial Derivatives

The partial derivatives in Equation 9 are computed using the DSM (Kawai et al., 2006) down to 3.2 s, using the formulation of Geller and Ohminato (1994); the partial derivatives with respect to Q_S^{-1} are as defined in Fuji et al. (2010). The current version of DSM allows only computation of (exact) synthetics and partial derivatives for spherically symmetric (1-D) velocity models. The obvious advantage is that it allows us to use higher frequencies than with 3-D wave propagation codes, which is important for the study of the D'' region because seismic phases due to interactions with the D'' discontinuity are visible only at relatively high frequencies.

The partial derivatives for the spectral amplitude misfit in Equation 10 are computed using the chain rule:

$$\frac{\partial \ln |\tilde{\mathbf{s}}|_i}{\partial m_j} = \frac{1}{|\tilde{\mathbf{s}}|_i^2} \left(\Re(\tilde{\mathbf{s}}_i) \frac{\partial \Re(\tilde{\mathbf{s}}_i)}{\partial m_j} + \Im(\tilde{\mathbf{s}}_i) \frac{\partial \Im(\tilde{\mathbf{s}}_i)}{\partial m_j} \right), \quad (14)$$

where $\Re(\tilde{\mathbf{s}})$, and $\Im(\tilde{\mathbf{s}})$ denote the real, and imaginary parts of $\tilde{\mathbf{s}}$, the Fourier transform of the synthetics \mathbf{s} .

3.3. Travel Time Corrections

We use the S phase as a reference phase to correct ScS travel times for the 3-D structure above our explored region by aligning the onset of the S waves on the data and synthetics (Fuji et al., 2010). The ScS - S differential travel time, however, also includes the effects of the 3-D structure near S waves turning points. Ventosa and Romanowicz (2015) showed that corrections to the PcP - P differential travel time using global tomographic models can be large, and should be taken into account when studying the structure of the lowermost mantle. We therefore apply an additional travel time correction based on the global model SEMUCB_WM1. We truncate SEMUCB_WM1 at 2,500 km depth to exclude the 3-D structure within our explored region, and use it to compute differential ScS - S travel times (for raypaths computed using TauP; Crowell et al., 1999). The additional travel time correction is obtained by subtracting the ScS - S differential travel time for the 3-D model to that for PREM.

3.4. Amplitude Corrections for Focusing due to Out-Of-Plane V_S Anomalies

One contribution of this study is the use of amplitude corrections for focusing effects due to out-of-plane V_S variations in D'' . We separate the contribution to focusing into three components: two in-plane contributions due to V_S anomalies (a) in the vertical direction, and (b) along the source-receiver direction; and the out-of-plane contribution due to lateral V_S anomalies.

The effect of vertical V_S anomalies is already accounted for in our 1-D inversion, but the remaining in-plane and the out-of-plane contributions are not. Since we infer 1-D V_S models in several contiguous corridors, it is possible to use these models to quantify the contribution to focusing from out-of-plane V_S anomalies. On the other hand, our 1-D models cannot be used to quantify the contribution from anomalies along the source-receiver. We thus concentrate in this study on the out-of-plane contribution to focusing. This is in part justified because of the geometrical setting of our data set: the incidence angles of ScS phases at the CMB are close to horizontal, between $\sim 70^\circ$ and $\sim 77^\circ$ (as computed for PREM), which implies that vertical V_S anomalies contribute to focusing ~ 2.7 to ~ 4.3 times (as given by the tangent of the incidence angle) more than anomalies along the source-receiver direction (focusing is proportional to the second derivative in the direction perpendicular to the raypath). We note that this might not be the case if strong small-scale 3-D low-velocity anomalies are present above the CMB in the explored region, for example, ultra-low velocity zones (ULVZs), which bend raypaths toward the vertical. However, while our region of interest has been extensively explored by recent studies using high-quality USArray data (Ko et al., 2017; Whittaker et al., 2015; Yu et al., 2014), none of these studies have observed an ULVZ in our explored region. As an exception, Thorne et al. (2019) reported a potential ULVZ using SKS waveforms, but its location could only be constrained to either within our study region, or within the LLSVP beneath Africa because of the use of a single event and limited azimuthal coverage for this particular region. Given that most ULVZs observed so far are located at the edges, or within LLSVPs, a location beneath Africa appears more likely in this case. We show below that focusing effects due to out-of-plane V_S anomalies are significant, due to the presence of a low-velocity corridor surrounded by two high-velocity regions.

In order to evaluate, and correct for, the out-of-plane contribution, we use synthetics computed using SPEC3D for two 3-D V_S models representative of the structure in our explored region for clusters S and N. These models were obtained by combining inverted 1-D V_S models in each corridor. Before combining the 1-D models, we first average them by region, which resulted in four 1-D models for high- and low-velocity regions for clusters S and N (Figures 2c and 2f). The average is taken in order to focus on the most significant feature in the explored region (a low-velocity corridor surrounded by two high-velocity regions), and does not significantly affect the amplitude corrections. The SPEC3D synthetics are computed for one event in each cluster (events #19 and #22 in Table S1) down to 7.1 s, and filtered with a bandpass filter between 12.5 and 200 s. We then measure amplitude ratios for the ScS phase between the SPEC3D and PREM synthetics, and between the synthetics for the 1-D inverted V_S models and PREM.

Figures 2a and 2d show the amplitude ratios for the ScS phase between SPEC3D and PREM synthetics. These ratios contain contributions from both lateral and vertical V_S anomalies. We note the strong focusing within the low-velocity corridors S3 and N4, and defocusing in adjacent corridors. This pattern is consistent with the prediction from ray theory (Woodhouse & Wong, 1986), since the second derivative of V_S in the out-of-plane direction is positive within low-velocity corridors (resulting in focusing), and negative at their edges (resulting in defocusing).

The contribution from vertical V_S anomalies only is given in Figures 2b and 2e, which show the amplitude ratios between synthetics for the 1-D inverted V_S models and PREM. We note the strong dependence on epicentral distance, with an increase in defocusing for the high-velocity corridors at distances larger than $\sim 71^\circ$, due to the interaction of the ScS phase with the D'' discontinuity at near-critical angles. Such a strong variation with distance for the out-of-plane contribution to focusing is not expected, since the V_S gradient in the out-of-plane direction does not vary significantly with increasing distance.

In order to isolate the amplitude effect due to out-of-plane V_S anomalies only, we take the ratio between the SPEC3D synthetics and the synthetics for the 1-D inverted V_S models. Furthermore, we use only the records in the distance range 65° – 71° , where the contribution from vertical V_S anomalies is still relatively small. For each corridor and each cluster, we then take the average of the ScS amplitude ratios, and define

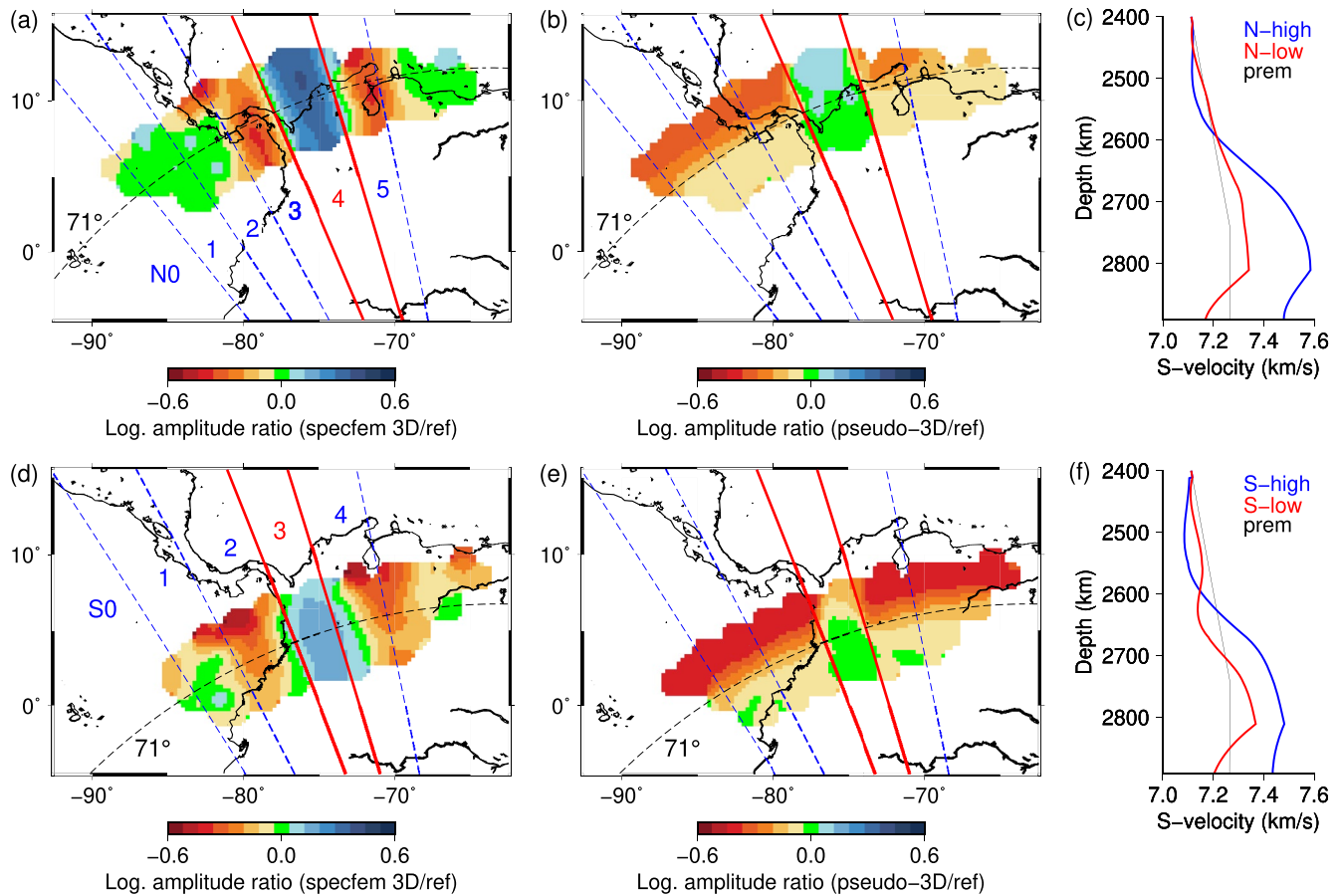


Figure 2. Focusing of the ScS wave due to lateral V_5 variations in D'' . Panels (a–c) are for cluster N; panels (d–f) are for cluster S. The 3-D velocity models for clusters N, and S are defined using the 1-D profiles in panels (c) and (f), respectively. Panels a and d show the (log of) ScS amplitude ratio between 3-D synthetics computed using SPECFEM3D and synthetics for PREM. Panels b and e show the (log of) amplitude ratio between 1-D synthetics computed for the low-velocity profiles in corridors N4 and S3, and high-velocity profiles in the remaining corridors, and PREM. The curved dashed black line indicates 71° of epicentral distance from the source.

the amplitude correction as the inverse of this average ratio. The resulting corrections are given by: (N0, N1, N2, N3, N4, and N5) = (0.93, 0.93, 0.93, 1.12, 0.80, and 1.11) for cluster N, and (S0, S1, S2, S3, and S4) = (1.00, 1.00, 1.05, 0.86, and 1.06) for cluster S.

As mentioned above, the corrections are computed using synthetics with a minimum period of 12.5 s, which is intermediate between the minimum period of 8 s used for the actual inversion, and the maximum period of 25 s for the spectral amplitude ratios. The frequency dependence of the amplitude ratios is shown in Figure S2, and indicates that the amplitude anomalies generally decrease as the minimum period increase. For instance, the amplitude ratio for the low-velocity corridor S3 is 1.18 at 8 s, 1.16 at 12.5 s, and 1.10 at 20 s (Figure S2c). This decrease with frequency suggests that corrections should be computed at an intermediate period between the minimum and maximum periods used in the actual inversion. We show below that this is a reasonable assumption.

In Figure S3, we check the validity of using a single correction for each corridor, averaged over epicentral distances and computed at an intermediate frequency. We conduct a synthetic test using as input data the same SPECFEM3D synthetics as in Figure 2d, and sampling the low-velocity corridor S3. For this test, the minimum period is 12.5 s. We compare the recovered models after 1-D inversion without using amplitude corrections to those using corrections measured at 12.5, 16, and 20 s. The results show an artificially high Q_5 (~390) at the CMB when amplitude corrections are not used. When using corrections at 12.5, 16, and 20 s, the recovered vertically averaged Q_5 is respectively slightly smaller, nearly equal, and slightly larger than

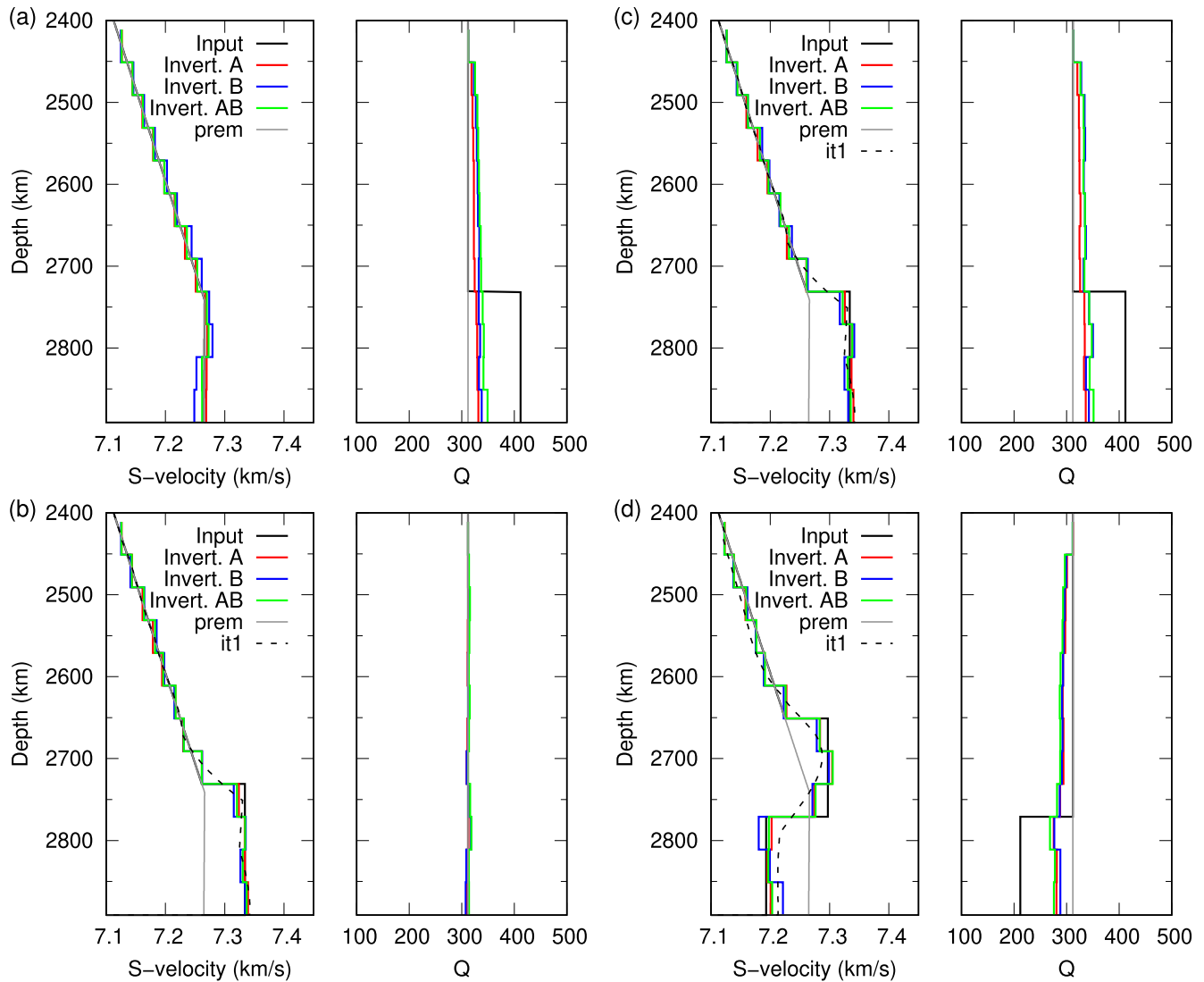


Figure 3. Resolution tests for four different input structures (a)–(d) (black lines). For all inputs, the perturbations are (in absolute value) 1% for V_S and 100 for Q_S , and the thickness of perturbed layers is 160 km in panels (a)–(c), and 120 km in panel (d). The recovered models after inversion are shown in red (using the waveform misfit only; labeled A), blue (using the spectral amplitude misfit only; labeled B), and green (using both misfits; labeled AB). For panels (b)–(d), we performed two iterations to first recover V_S (black dashed lines, labeled “it1”), and then V_S and Q_S . The input synthetics are computed exactly (using DSM) for the input models, and thus include non-linear effects (in contrast to the usual checkerboard test).

that of PREM. This suggests that the use of corrections averaged over epicentral distance and computed at an intermediate frequency is appropriate.

4. Resolution Tests

We perform synthetic resolution tests in order to verify the ability of our methods to recover both the V_S and Q_S structures (Figure 3). We compute synthetics for four input structures (black lines in Figure 3), and check how well the inversion recovers these known input structures. The synthetics are filtered between 8 and 200 s, as in the actual inversion, and the data set is the same as that for corridor S3. Note that the synthetics for the input structures are computed exactly using the DSM, and thus include non-linear effects (in contrast to usual checkerboard tests), which makes the recovery of input models more difficult, but also more representative of the actual resolution.

We use the same regularization parameters as in the actual inversion for the high-velocity corridors for cluster S (see Results). This implies a relatively large smoothness regularization value for the Q_S structure $\lambda_q = 0.16$, which effectively results in our inversion being able to resolve only an average Q_S value throughout the depth of our models. In the actual inversion, this large λ_q values are required to avoid unstable Q_S structure that may occur because of (a) the relatively small effect of Q_S on the waveforms compared to that of V_S (with trade-offs between the two), and (b) the fact that the 1-D V_S structure cannot perfectly fit the ScS travel times due to presence of small-scale 3-D structures, inducing small-scale artifacts in Q_S due to trade-offs with V_S .

Results of the tests (Figure 3) show that the V_S structure is well constrained using both the waveform misfit, the spectral amplitude misfit, and the combination of both. The Q_S structure is more difficult to resolve, but its radially averaged value is relatively well constrained. The ratios of the average Q_S between the recovered and initial models in panels (a), (c), and (d), are 0.73, 0.77, and 1.07, respectively. The waveform misfit performs slightly better than the spectral amplitude misfit for the V_S structure, but slightly worse for the Q_S structure. Furthermore, the spectral amplitude misfit performs much better at recovering the Q_S structure when the initial V_S structure is far from the actual V_S structure (see Figure S4), and therefore should provide more robust Q_S models.

5. Results

5.1. Inferred V_S and Q_S Models

Figure 4 shows our preferred models, which include corrections for 3-D focusing effects. The V_S models are generally consistent with the trend in travel times observed in Figure 1. The only exception is corridor N4, for which the travel times residuals in Figure 1 are slightly positive (0.43 s), but whose average V_S is 0.1% faster than PREM. Note, though, that validity checks in Section 5.5 show improvements to the variance and cross-correlation misfits for corridor N4 (the improvement is small because the structure in corridor N4 is close to that of PREM). This discrepancy could be due to uncertainties in the measured differential travel times in Figure 1, and the fact that travel times in Figure 1 were measured at 12.5 s, but the actual inversion use minimum periods of 8 s. In addition, this could be due to the fact that we do not explicitly use a travel time misfit in the inversion. Although we usually expect that an improvement in variance or cross-correlation misfits would also result in an improvement in the travel time misfit, some amount of waveform distortion could make this assumption invalid, which is what seems to happen for corridor N4 (see waveforms in Figure S8b). We emphasize that this discrepancy is apparent in corridor N4 because of the small average travel time anomalies (0.43 s) with respect to the initial model, PREM.

We display our models into four groups, with the high-velocity corridors for clusters N and S shown in panels (a) and (c), and the low-velocity corridors shown in panels (b) and (d), respectively. Each model is shown as a thick filled region, representing estimated model uncertainties due to the choice of regularization parameters. The number of iterations to obtain the final models are: 1 for the low-velocity corridors N4 (Figure 4b) and S3 (Figures 4d), 2 for the high-velocity corridors of cluster S (Figure 4c), and 3 for the high-velocity corridors of cluster N (Figure 4a). After each iteration, we visually inspected the waveforms and inverted models. We stopped the iterations when (a) the inverted model did not differ significantly from that at the previous iteration, and (b) the arrival times of ScS waveforms peaks on observed waveforms and synthetics for the previous iteration were close, in which case the Born approximation can be used.

In the high-velocity corridors, V_S models show similar features within each cluster (S and N), but with some variability ($\sim 0.8\%$) within 80 km of the CMB. Model N5 differs the most, most likely due to the fact that only 66 records were available to constrain this model. Differences in the Q_S models is generally within the uncertainty on Q_S . In the remaining of this study, we discuss average values for the models in each sub-groups, but exclude model N5 since it is not as robust as the models for the other corridors. At 90 km above the CMB, average increases in V_S (with respect to PREM) in high-velocity corridors are 3.5% (cluster N), and 2.1% (cluster S), while average Q_S values over the depth range of our models are 445 (cluster N), and 438 (cluster S). Note the relatively broad, large velocity increase from $\sim 2,551$ to 2,791 km depth (i.e., 340–100 km above the CMB), with a total increase of 4.5% (cluster N), and 4.4% (cluster S). For comparison, in the same depth range PREM increases by 1.2%. The profiles for event cluster N (panel a) show a decrease in V_S within

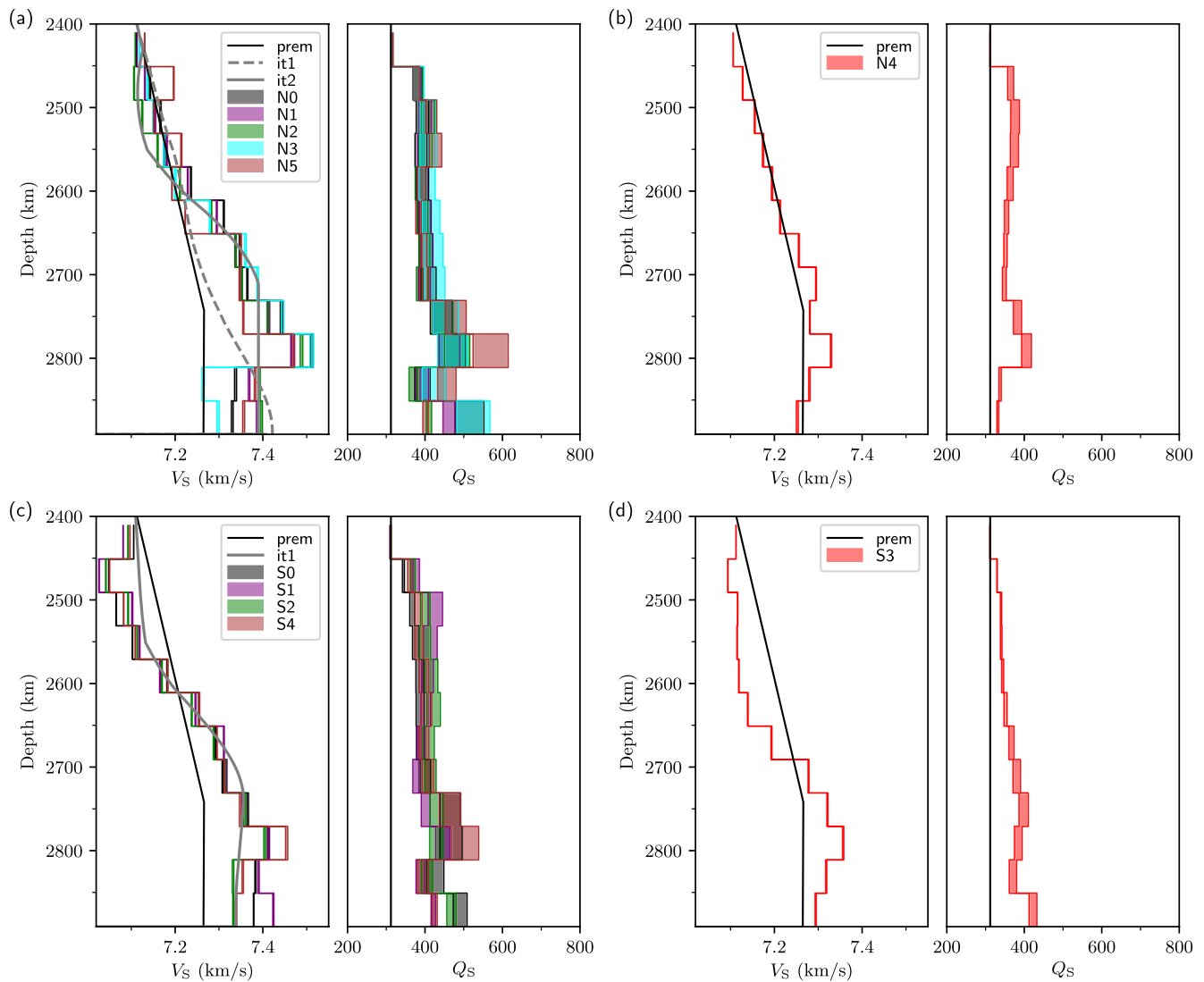


Figure 4. Models obtained after iterative inversion for V_S and Q_S , and after correcting for focusing effects. Panels (a) and (b) show the high-, and low-velocity regions for event cluster N. Panels (c) and (d) show the high-, and low-velocity regions for cluster S. The labels S0 to S4 and N0 to N5 correspond to the corridors in Figure 1. The initial model (PREM) is shown in gray solid lines; the intermediate V_S models (for panels (a) and (c)) are shown in gray dashed lines. The final models and their estimated uncertainties (due to the inversion parameters) are shown by thick colored curves.

90 km above the CMB of -2.5% in average. For cluster S, a decrease in V_S is also present, but is much weaker. This sharp decrease close to the CMB causes an amplification of the ScS waves and is mostly constrained by the spectral amplitude misfit.

The low-velocity corridor N4 (panel b) has a V_S close to PREM, with a slightly negative gradient within 90 km above the CMB. In contrast, the low-velocity corridor S3 (panel d) shows low V_S (minimum -1.1%) in the range 2,400–2,651 km depth, followed by a relatively steep increase, $\sim 3.3\%$, from 2,631 to 2,791 km depth (i.e., 260–100 km above the CMB). The presence of a steep increase in V_S for corridor S3 and not for corridor N4 reflects the presence of a clear Scd phase in the data for corridor S3, but not for corridor N4. For both corridors S3 and N4, Q_S is slightly higher than PREM, with average values over the depth range of our models of 391 (N4), and 395 (S3). These values are lower than for the high-velocity corridors, although still higher than PREM.

The large velocity increases in models for the high-velocity regions and for the low-velocity corridor S3 correspond to the D'' discontinuity. As mentioned above, the depth at which V_S starts to increase is ~ 80 km

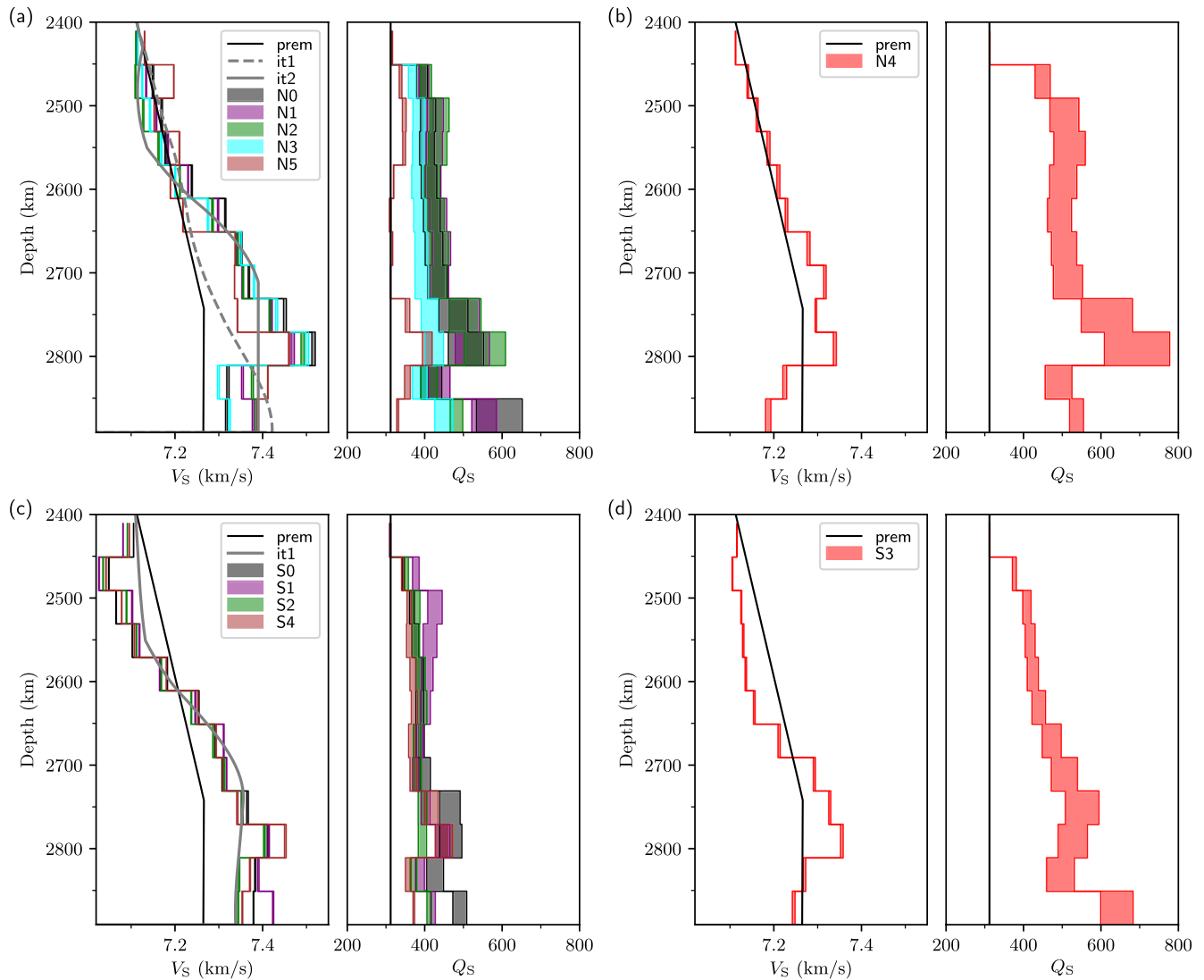


Figure 5. Same as Figure 4, but without corrections for focusing effects.

shallower for the high-velocity corridors (340 km above the CMB for panels a and b) than for the low-velocity corridor S3 (260 km above the CMB).

5.2. Effect of Corrections for Focusing

To illustrate the importance of correcting for focusing effects, we calculated models without corrections (Figure 5). In that case, the average value of Q_S over the depth of our models increases from 391 to 558 for corridor N4, and from 395 to 506 for corridor S3. In addition, V_S decreases from 7.25 to 7.18 km/s in corridor N4, and from 7.29 to 7.25 km/s in corridor S3. In uncorrected models, the increase in Q_S and decrease in V_S at the CMB both contribute to increase the amplitude of ScS waves on synthetics so that they can match the observed ScS amplitudes, which are being amplified by propagation through a low-velocity trough.

Because of their large Q_S values, uncorrected models S3 and N4 do not have a reasonable interpretation in terms of temperature (Section 6.3). Taking into account focusing effects due to propagation within a low-velocity trough allows a coherent interpretation of these models in terms of temperature and pPv fraction changes. These results thus indicate that corrections for 3-D focusing effects should be performed to obtain a reasonable interpretation of the Q_S and V_S structures for D'' beneath Central America. Note that such

corrections might not be as important for regions of the lowermost mantle where strong small-scale velocity heterogeneities are not present, for example, regions without slabs at the CMB, as in Konishi et al. (2017).

5.3. Choice of Regularization Parameters

We chose the smoothing parameters λ_v and λ_q , and the damping γ_v on V_S by trying a range of values and visually inspecting inferred models and the change in misfit. We set $\lambda_v = 0.01$, $\lambda_q = 0.16$, and $\gamma_v = 0.01$ for all corridors, except for corridor S5, where $\lambda_q = 0.64$ and $\gamma_v = 0.04$ (this larger value being due to the small number of records, 66, for corridor S5).

Among all the damping parameters, γ_q has the largest influence on the inferred Q_S models. We therefore used L-curves (which provide a more quantitative approach) to find the “optimal” γ_q . The L-curves are computed for each corridor, and shown in Figure S5. Based on the L-curves, we set $\gamma_q = 0.79$ for all corridors for cluster S, $\gamma_q = 1$ for corridors N1, N2, N4, $\gamma_q = 1.99$ for corridor N0, and $\gamma_q = 2.79$ for corridor N3. The large value for corridor N3 is partly due to the amplification factor of $1/0.93$ applied to correct for defocusing in the corridors directly adjacent to the low-velocity corridor N4.

5.4. Uncertainties on V_S and Q_S

An estimation of the uncertainties on the V_S and Q_S structures is important in order to use our models to constrain the temperature and amount of pPv in the lowermost mantle. Uncertainties have several sources, including, in our case, errors in the forward modeling parameters and data pre-processing (source parameters, corrections for the structure above our target region, corrections for 3-D focusing effects), and uncertainties in the formulation of the inverse problem (values of β , and of the regularization parameters).

The latter source of uncertainties can be estimated by varying the parameters of the inverse problem. Since γ_q has the largest effect on the inferred models, we estimate the model uncertainties by conducting three inversions for each corridor, varying γ_q by $\pm 25\%$ around its “optimal” value. The resulting range of Q_S values for each corridor is represented by filled regions in Figure 4, and is generally between 20 (for Q_S values closer to PREM) and 100 (for Q_S values further from PREM). The V_S structure is also slightly affected by varying γ_q , as a result of the trade-off between Q_S and V_S .

5.5. Validation of Inferred Models

We assess the validity of our models by checking the improvement in the fit to the data between synthetics for our models (Figure 4) and those for PREM. To allow direct comparison between corridors, the variance reduction is normalized by the initial variance for each corridor, and is given by

$$\begin{aligned} \text{V.R.} &= 1 - \frac{\phi(\mathbf{m}^{\text{final}})}{\phi(\mathbf{m}^{\text{prem}})} \\ &= 0.5 \left(1 - \frac{\phi_A(\mathbf{m}^{\text{final}})}{\phi_A(\mathbf{m}^{\text{prem}})} \right) + 0.5 \left(1 - \frac{\beta \phi_B(\mathbf{m}^{\text{final}})}{\phi_A(\mathbf{m}^{\text{prem}})} \right), \end{aligned} \quad (15)$$

where ϕ is as defined in Equation 4, and the last equality holds because $\beta = \phi_A(m^{\text{prem}}) / \phi_B(m^{\text{prem}})$ (see Text S3).

Figure 6 shows the variance reductions averaged for the high- and low-velocity corridors for clusters N and S (Figure 4). The three columns show the variance reduction when considering both the V_S and Q_S structure (left column), and the separate contributions from the V_S (middle column) and Q_S (right column) structures only. Note that the sum of the contributions from V_S and Q_S only is not equal to the variance reduction for the joint V_S and Q_S models, because of the trade-off between V_S and Q_S . We also show separately the contribution from the waveform misfit (labeled A) and the spectral amplitude misfit (labeled B). The total variance reduction is the sum of both contributions (see Equation 15). Note the factor 0.5 in Equation 15, which implies that the separate contributions to the variance reduction in Figure 6 are half of that for a single-objective function (e.g., waveform misfit only).

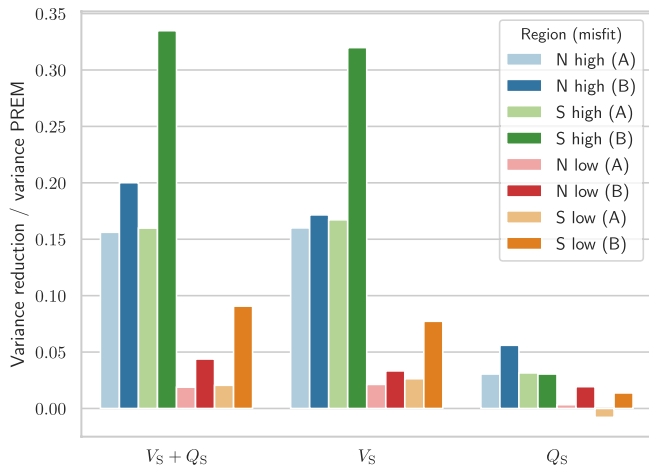


Figure 6. Variance reduction normalized to the variance for PREM synthetics (Equation 15). Variance reductions are averaged for each group of corridors (high- and low-velocity corridors for clusters N and S) in Figure 4. The variance reduction is shown separately for the waveform misfit (labeled A), and spectral amplitude misfit (labeled B). The total variance reduction is the sum of both. Column $V_S + Q_S$ shows the actual variance reduction for models in Figure 4; columns V_S , and Q_S show the variance reduction when using only the inferred V_S , or Q_S structure, respectively, and are shown for the purpose of discussion.

The total variance reductions when considering both the V_S and Q_S structures range from $\sim 7\%$ for corridor N4, to $\sim 50\%$ for the high-velocity corridors for cluster S. When considering only the Q_S structure, the variance reduction is always smaller than when considering only the V_S structure. This shows the dominant influence of V_S in the inversion, and is one reason why the uncertainty on Q_S models is larger than on V_S models. However, the variance reduction due to the Q_S structure only is still significant, which suggests that the data contain information about the Q_S structure.

The variance reduction for the spectral amplitude misfit is always larger than that for the waveform misfit. The relative amount of variance reductions can be changed by varying the parameter β in Equation 4, with a smaller β resulting in models that are more dominated by the waveform misfit. For most of the corridors, the variance reduction for both the waveform and spectral amplitude misfits are, however, large, which suggest that our choice of β is reasonable. The influence of β on the inversion results, possibly adding additional objective functions, still needs to be investigated in details. Here, we only note that the spectral amplitude misfit tends to result in models with stronger variations in velocity gradients, since these gradients affect waveform amplitudes. In particular, the low-velocity gradients right above the CMB (strongest for models in Figure 4a) are mostly constrained by the spectral amplitude misfit.

Additional comparison of improvements to waveform are shown in the Supporting Information. Figure S6 shows improvements to the distributions of ScS amplitude ratios between synthetics and observed waveforms, of variances, and of cross-correlation coefficients. For all regions except corridor S3, the distribution of amplitude ratios is improved (shifted toward 1) when compared to PREM. Our model for corridor S3 shows roughly the same amplitude ratios as that for PREM. The distributions of variance and cross-correlations are also improved for all regions (i.e., shifted toward lower values, and toward 1, respectively), with the largest improvements seen for the high-velocity regions. One reason for the smaller fit improvement for regions S3 and N4 is that their structure is closer to that of the initial model (PREM). For corridor S3, another reason is shown in Figure S7, which shows the improvement in waveform fit and amplitude ratios as a function of the epicentral distance. Figure S7 shows that the waveform fit for region S3 is slightly worse than for PREM for epicentral distances smaller than 74° . This is also the case for corridor S2 for distances larger than 75° , and probably indicates the presence of V_S variations along the source-receiver directions for these two corridors.

Figure S8 shows four record sections of stacked waveforms for the high-velocity corridors N0 and S1, and the low-velocity corridors N4 and S3. As noted above, the high-velocity corridors show the clearest improvement in both the travel time and amplitude of the ScS phase. Corridors N0, S1, and S3 also show improvement to the fit of the Scd phase, which is due to interaction with the D'' discontinuity. The Scd travel time is nearly perfectly fit, while the Scd amplitude fit varies between corridors and epicentral distance: the fit is relatively good for corridor N0 for all distances, and for corridor S1 at epicentral distances between 73° and 74° . At other distances, the amplitude of observed Scd phases is larger than the amplitude predicted by our models. This could indicate that the D'' discontinuity in the southern clusters is either sharper, or with a stronger V_S increase than in our models. Our model for corridor N4 does not produce an Scd phase (as it has no steep increase in V_S). This seems consistent with the observed waveforms in Figure S8b, which do not show a clear ScS precursor. We note that without the waveform for our inferred models (green traces), it might have been difficult to identify the Scd phase without further processing, because of noise in individual waveforms. This illustrates an advantage of waveform inversion, which can infer the presence of a Scd phase without a priori assumptions, since the Scd phase is already accounted for in the waveform kernels. As noted above, corridors S1, S3, and N4 show that our 1-D models cannot completely fit ScS travel times and amplitudes for all epicentral distances, which is indicative of some amount of 3-D V_S , and possibly Q_S , anomalies within these corridors. We note that the stacked waveforms in Figure S7 do not give a precise

comparison of improvement to ScS amplitudes (instead, Figure S6 does). This is because amplitudes of stacked waveforms are inevitably smaller for observed data than for synthetics because predicted arrival times are used to align waveforms.

6. Discussion

6.1. Comparison to Previous Studies

Several studies have used waveform modeling, array analysis (Whittaker et al., 2015), grid-search (Ko et al., 2017), localized finite-frequency travel time tomography (Hung et al., 2005), and localized waveform inversion (Borgeaud et al., 2017; Kawai et al., 2007) to determine the 1-D and 3-D V_S structure of the lowermost mantle beneath Central America. Fewer studies inferred the Q_S structure in this region, all of which used ScS-S differential δt^* (Durand et al., 2013; Fisher et al., 2003; Ford et al., 2012).

Ford et al. (2012) studied the Q_S structure in a region just north of corridors N0 and N1, and found large negative δt^* , suggesting high (apparent) Q_S in the lowermost mantle. This is generally consistent with the high Q_S structure seen in our models (Figure 4). Ford et al. (2012) pointed out that the δt^* they measured are too small to be explained by the Q_S structure of D'' only, and they suggested that this could be due to anomalies in S waves amplitudes. This agrees with our observations that the S waves amplitudes are affected by a complex 3-D mid-mantle structure due to the Farallon slab (Figure S1).

Fisher et al. (2003) studied the V_S and Q_S structures of D'' in a region that roughly corresponds to corridors S2–S4 to N2–N5. They found patches of high and low V_S and Q_S , with V_S and Q_S perturbations being overall positively correlated, but not perfectly (some regions being negatively correlated). By contrast, we do not see low Q_S regions in our models, but we observe smaller Q_S for the low-velocity corridors S3 and N4. Note that the most prominent low Q_S patch in Fisher et al. (2003) is located in the gap between bouncing points for our S and N clusters. Fisher et al. (2003) travel time pattern also slightly differ from ours. Possible reasons for these discrepancies include differences in data set (Fisher et al., 2003 data coming mainly from two linear temporary arrays in northeastern US), and methods. In particular, Fisher et al. (2003) did not perform travel time corrections for the 3-D mantle, and used ScS/S amplitude ratios, which are potentially contaminated by variations in S-wave amplitude due to the subducting Farallon slab (Section 2.2 and Text S1).

Ko et al. (2017) used a grid-search approach to study the V_S structure of D'' in roughly the same region as our event cluster S. The pattern of lateral V_S anomalies they observe at the CMB is globally consistent with our results, with high V_S at the CMB except in a region that corresponds to the low-velocity corridor S3. However, they found smaller V_S just above the CMB. This difference may be explained by two facts. First, Ko et al. (2017) fixed V_S above D'' to PREM, while in our models V_S in this region is not fixed and is smaller than PREM; and second, they used amplitude information but did not invert for Q_S , possibly resulting in a stronger negative V_S gradient just above the CMB in order to increase the amplitude of the ScS waves on synthetics to match the data (Section 5.2). Ko et al. (2017) further reported that the D'' discontinuity in the same region as our low-velocity corridor S3 is ~80 km deeper than for regions corresponding to the high-velocity corridors S0–S2. This is, again, in good agreement with our results, which indicate that the D'' discontinuity for corridor S3 is ~80 km deeper than for corridors S0–S2. However, the absolute depth of the D'' discontinuity they found is ~160 km larger than in our results. One possible explanation for this discrepancy is that the depth of D'' discontinuity in Ko et al. (2017) is constrained by Scd-S differential travel times, while in our study it is mostly constrained by Scd-ScS differential travel times. For comparison, note that Whittaker et al. (2015) reported a D'' discontinuity ~150–200 km above the CMB in the region of corridor S3, which is roughly in-between our results (260 km), and those of Ko et al. (2017) (100 km).

6.2. Limitations of Our Models

The V_S structure is well constrained in the inversion (i.e., there is no large dependence on the regularization parameters), but could suffer from errors in travel time corrections for the 3-D mantle and, to some extent, in the source moment magnitude, since we also use a spectral amplitude misfit. Note, however, that the latter is mitigated by the use of a relatively large number of earthquakes, and the presence of multiple phases (ScS and Scd) in our time windows with nearly identical sensitivities to the shallow mantle.

Table 1
Temperature Perturbations (in Kelvin) Obtained From Models in Figure 4, Using the Values Within 40 km Above the CMB

Region	dT_{V_S} [K] (0–40 km)	dT_{Q_S} [K] (0–480 km)
N high	–434	–195
S high	–511	–184
N low (N4)	62	–104
S low (S3)	–144	–110

Abbreviation: CMB, core-mantle boundary.

In addition, the Q_S structure may suffer from its stronger dependence on the damping parameter γ_q , uncertainties in the mid-mantle and upper mantle Q_S , and uncertainties on the corrections for focusing effects. If present, strong, small-scale 3-D structures in our target region, such as ULVZ (Thorne et al., 2019), or strong small-scale scatterers (Takeuchi et al., 2017), could also affect the amplitude of ScS waveforms, and is not modeled in this study. Also, note that our corrections for focusing effects are not perfect. 3-D full-waveform inversion is needed to account more accurately for the trade-off between V_S and Q_S related to 3-D focusing effects. However, even 3-D full-waveform inversion could underestimate focusing effects, since these effects depend on the second derivative of the velocity field, which is underestimated when regularization is used.

6.3. Constraints on the Temperature and Presence of pPv

Our V_S and Q_S models give two types of constraints on the temperature of the lowermost mantle. First, assuming that Q_S is mostly sensitive to temperature, its lateral variations in the lowermost mantle provide an estimate of the temperature variations in this region. Second, variations in the depth of the D' discontinuity can be translated to variations in temperature using published values for the Clapeyron slope of the Bridgmanite to pPv phase transition (Ko et al., 2017; Whittaker et al., 2015). Following Deschamps et al. (2019) the temperature perturbation required to explain the V_S perturbations $d \ln V_S$ (with respect to PREM) at a given depth is

$$dT_{V_S} = \frac{d \ln V_S - S_{pPv} dX_{pPv}}{S_T}, \quad (16)$$

where dX_{pPv} is the anomaly in pPv fraction (with respect to its horizontal average value), $S_{pPv} = 0.02$ is the sensitivity of V_S to the volume fraction of pPv, and $S_T = 2.8 \cdot 10^{-5} \text{ K}^{-1}$ is the temperature sensitivity of V_S . The temperature perturbation explaining the inferred Q_S is given by

$$dT_{Q_S} = -\frac{RT_{ref}}{\alpha H} \frac{\ln \frac{Q_S}{Q_{ref}}}{1 + \frac{RT_{ref}}{\alpha H} \ln \frac{Q_S}{Q_{ref}}}, \quad (17)$$

where R is the ideal gas constant, $H = 495 \text{ kJmol}^{-1}$ is the activation enthalpy, $T_{ref} = 3440 \text{ K}$ is an average reference temperature in the lowermost 500 km of the mantle assuming an adiabatic gradient (defined as the horizontally averaged temperature), $\alpha = 0.274$ is the exponent for the frequency dependence of Q_S , and $Q_{ref} = 312$ is PREM Q_S . See Deschamps et al. (2019) for details on the values for the physical parameters. It should be kept in mind that these parameters are poorly constrained.

Table 1 lists the temperature perturbations obtained from our inferred V_S and Q_S models, assuming no pPv (i.e., $dX_{pPv} = 0$) and no chemical heterogeneities. Based on the results of the checkerboard tests, which show that only the radially averaged Q_S can be resolved, we use the average of Q_S over the depth range of our models to compute dT_{Q_S} . For dT_{V_S} , we use the V_S perturbation within 40 km above the CMB. The difference in resolution between V_S and Q_S makes a direct comparison difficult. Despite the lack of radial resolution in Q_S , the resolution tests we performed indicate that the values of Q_S we inferred are a good estimate of the radially averaged attenuation in each corridor. Note that uncertainties on Q_S remain due to its strong dependence on focusing effects, although we did our best to correct for these effects. The difference in the Q_S we observe should thus be representative of the radially averaged temperature anomalies between the cold and the warm regions. As one would expect, inferred temperatures are lower in high-velocity corridors (with dT_{Q_S} around -184 K and -195 K) than in low-velocity corridors (with dT_{Q_S} around -104 K and -110 K in corridors N4 and S3, respectively).

Table 1 further indicates strong discrepancies between the temperature anomalies inferred from V_S and Q_S . At least part of this disagreement may be solved when accounting for uncertainties in the modeling parameters of dT_{Q_S} . However, a close examination at Table 1 indicates that the temperature predicted by Q_S

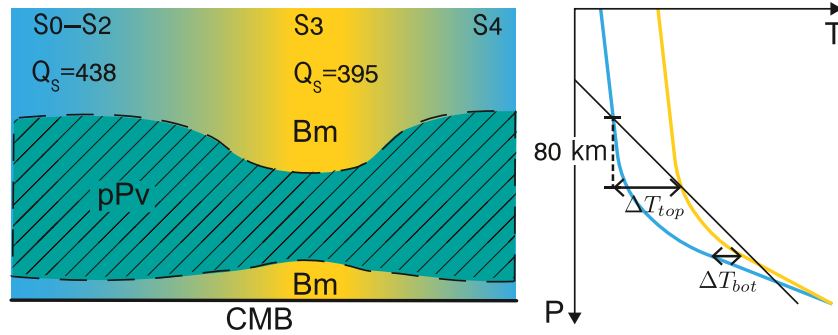


Figure 7. Schematic interpretation of our models. The left panel shows a schematic cross-section of the lowermost mantle for corridors S0 to S4, with the background colors showing variations in temperature. The right panel shows two possible geotherms for the cold (S0-S2 and S4) and warm (S3) regions on top of the Bridgemanite (Bm) to post-Pervoskite (pPv) phase diagram.

are significantly larger than those predicted by V_S ($dT_{Q_S} > dT_{V_S}$) in high-velocity regions, but are closer (for S low), or lower ($dT_{Q_S} < dT_{V_S}$) (for N low) in low-velocity regions, suggesting that uncertainties in dT_{Q_S} may not explain all the observed discrepancies. Interestingly, this trend is consistent with the positive Clapeyron slope of the Bridgemanite to pPv phase transition. Since low-velocity regions are hotter, the amount of pPv in these locations should be smaller than in high-velocity regions (for instance, because pPv transforms back to Bridgemanite at shallower depths). In high-velocity regions, V_S is therefore more affected by the presence of pPv, whose effect is to increase V_S (Cobden et al., 2015; i.e., S_{pPv} in Equation 16 is positive). If pPv is not accounted for when estimating dT_{V_S} , these regions will appear colder than they are.

As discussed in Section 6.1, the D'' discontinuity in model S3 is ~80 km deeper than for the models in the high-velocity regions (S0 to S2). This difference in depth can be explained by a temperature difference of about -250 to -750 K between the local geotherms at a depth of ~2,600 km for Clapeyron slopes between 7.5 MPa/K (Tsuchiya et al., 2004) and 13 MPa/K (Oganov & Ono, 2004), respectively, and assuming a ± 20 km uncertainty on the depth of the D'' (corresponding to the radial thickness of our model parameters). This temperature difference is larger than that estimated from variations in Q_S . A possible explanation for this is given in Figure 7, which summarizes the interpretation of our models. Since the geotherms for the cold and warm corridors have the same temperature at the CMB, the temperature difference at the CMB is smaller than at the top of the D'' layer. This makes the radially averaged temperature difference smaller than the temperature difference at the depth of the phase transition. This further implies the pPv lens is thinner in the warm (low-velocity) regions than in the cold (high-velocity) regions, that is, the average amount of pPv is larger in high-velocity corridors than in low-velocity corridors.

7. Conclusions

We used 1-D full-waveform inversion of ScS and Scd waveform data with a minimum period of 8 s from the USArray to constrain the V_S and Q_S structures in the lowermost 480 km of the mantle beneath Northern South America and Central America. We improved on previous studies by using a spectral amplitude misfit in addition to the waveform misfit, and showed that the former is more robust with respects to uncertainties in the initial V_S models, in agreement with Karaoğlu and Romanowicz (2018a). We found that ScS waveforms should be corrected for focusing effects resulting from the propagation of ScS waves through structures with significant lateral V_S variations in the region we sampled, and more specifically through a low-velocity corridor surrounded by high-velocity regions. After corrections, lateral variations in the inferred V_S and Q_S profiles are overall consistent with radially averaged lateral variations of temperature of ~75–90 K, and of ~250–750 K between the local geotherms at a depth of ~2,600 km. Discrepancies between the temperatures inferred from V_S and Q_S also suggest variations in the fraction of pPv above the CMB, with higher fractions in colder regions, and lower fractions in hotter regions. The methods developed in this study may be applied to other regions where strong 3-D focusing effects are expected, such as beneath

Hawaii (due to the presence of an ultra-low velocity zone), and open perspectives to better constrain the variations in temperature and composition above the CMB.

Conflict of Interest

The authors declare no conflicts of interest relevant to this study.

Data Availability Statement

The data used in this study are publicly available on the IRIS DMC server, and were collected using BREQ_FAST requests to IRIS DMC (http://ds.iris.edu/ds/nodes/dmc/manuals/breq_fast); the lists of events and networks necessary to request the data are shown in Tables S1 and S3. The data analysis was performed using the publicly available Klibrary package (Konishi & Borgeaud, 2020).

Acknowledgments

This study was funded by Academia Sinica grant AS-IA-108-M03. The authors thank two anonymous reviewers, the editor, and the associate editor for their attentive reading of the original manuscript and their constructive comments, which helped improve the current manuscript. We used the SPECFEM3D GLOBE c7.0.2 software, which was published under the GPL 2 license. This software was developed by the Computational Infrastructure for Geodynamics (<http://geodynamics.org>), which is funded by the U.S. National Science Foundation under awards EAR-0949446 and EAR-1550901.

References

- Anderson, D. L., & Given, J. W. (1981). Absorption band Q model for the Earth. *Journal of Geophysical Research*, 87(1), 3893–3904. <https://doi.org/10.1029/JB087iB05p03893>
- Borgeaud, A. F. E., Kawai, K., Konishi, K., & Geller, R. J. (2017). Imaging paleoslabs in the D'' layer beneath Central America and the Caribbean using seismic waveform inversion. *Science Advances*, 3(11), e1602700. <https://doi.org/10.1126/sciadv.1602700>
- Cobden, L., Thomas, C., & Trampert, J. (2015). Seismic detection of post-perovskite inside the Earth. In *The Earth's Heterogeneous Mantle* (pp. 391–440). Springer. https://doi.org/10.1007/978-3-319-15627-9_13
- Crotwell, H. P., Owens, T. J., & Ritsema, J. (1999). The TauP Toolkit: Flexible seismic travel-time and ray-path utilities. *Seismological Research Letters*, 70(2), 154–160. <https://doi.org/10.1785/gssrl.70.2.154>
- Deschamps, F., Konishi, K., Fuji, N., & Cobden, L. (2019). Radial thermo-chemical structure beneath Western and Northern Pacific from seismic waveform inversion. *Earth and Planetary Science Letters*, 520, 153–163. <https://doi.org/10.1016/j.epsl.2019.05.040>
- Durand, S., Matas, J., Ford, S., Ricard, Y., Romanowicz, B. A., & Montagner, J. (2013). Insights from ScS–S measurements on deep mantle attenuation. *Earth and Planetary Science Letters*, 374, 101–110. <https://doi.org/10.1016/j.epsl.2013.05.026>
- Dziewonski, A. M., & Anderson, D. L. (1981). Preliminary reference Earth model. *Physics of the Earth and Planetary Interiors*, 25(4), 297–356. [https://doi.org/10.1016/0031-9201\(81\)90046-7](https://doi.org/10.1016/0031-9201(81)90046-7)
- Ekström, G., Nettles, M., & Dziewonski, A. M. (2012). The global CMT project 2004–2010: Centroid-moment tensors for 13,1017 earthquakes. *Physics of the Earth and Planetary Interiors*, 200–201, 1–9. <https://doi.org/10.1016/j.pepi.2012.04.002>
- Fisher, J. L., Wyession, M. E., & Fischer, K. M. (2003). Small-scale lateral variations in D'' attenuation and velocity structure. *Geophysical Research Letters*, 30(8), 1–4. <https://doi.org/10.1029/2002GL016179>
- Ford, S. R., Garnero, E. J., & Thorne, M. S. (2012). Differential t^* measurements via instantaneous frequency matching: Observations of lower mantle shear attenuation heterogeneity beneath western Central America. *Geophysical Journal International*, 189(1), 513–523. <https://doi.org/10.1111/j.1365-246X.2011.05348.x>
- French, S. W., & Romanowicz, B. A. (2014). Whole-mantle radially anisotropic shear velocity structure from spectral-element waveform tomography. *Geophysical Journal International*, 199(3), 1303–1327. <https://doi.org/10.1093/gji/ggu334>
- Fuji, N., Kawai, K., & Geller, R. J. (2010). A methodology for inversion of broadband seismic waveforms for elastic and anelastic structure and its application to the mantle transition zone beneath the Northwestern Pacific. *Physics of the Earth and Planetary Interiors*, 180(3–4), 118–137. <https://doi.org/10.1016/j.pepi.2009.10.004>
- Geller, R. J., & Ohminato, T. (1994). Computation of synthetic seismograms and their partial derivatives for heterogeneous media with arbitrary natural boundary conditions using the Direct Solution Method. *Geophysical Journal International*, 116, 421–446. <https://doi.org/10.1111/j.1365-246X.1994.tb01807.x>
- Hung, S.-h., Garnero, E. J., Chiao, L.-y., Kuo, B.-Y., & Lay, T. (2005). Finite frequency tomography of D'' shear velocity heterogeneity beneath the Caribbean. *Journal of Geophysical Research*, 110(B7), 1–20. <https://doi.org/10.1029/2004JB003373>
- Hutko, A. R., Lay, T., Garnero, E. J., & Revenaugh, J. (2006). Seismic detection of folded, subducted lithosphere at the core-mantle boundary. *Nature*, 441, 333–336. <https://doi.org/10.1038/nature04757>
- Karaoğlu, H., & Romanowicz, B. (2018a). Global seismic attenuation imaging using full-waveform inversion: A comparative assessment of different choices of misfit functionals. *Geophysical Journal International*, 212(2), 807–826. <https://doi.org/10.1093/gji/ggx442>
- Karaoğlu, H., & Romanowicz, B. (2018b). Inferring global upper-mantle shear attenuation structure by waveform tomography using the spectral element method. *Geophysical Journal International*, 213(3), 1536–1558. <https://doi.org/10.1093/gji/ggy030>
- Kawai, K., Konishi, K., Geller, R. J., & Fuji, N. (2014). Methods for inversion of body-wave waveforms for localized three-dimensional seismic structure and an application to D'' structure beneath Central America. *Geophysical Journal International*, 197(1), 495–524. <https://doi.org/10.1093/gji/ggt520>
- Kawai, K., Takeuchi, N., & Geller, R. J. (2006). Complete synthetic seismograms up to 2 Hz for transversely isotropic spherically symmetric media. *Geophysical Journal International*, 164(2), 411–424. <https://doi.org/10.1111/j.1365-246X.2005.02829.x>
- Kawai, K., Takeuchi, N., Geller, R. J., & Fuji, N. (2007). Possible evidence for a double crossing phase transition in D'' beneath Central America from inversion of seismic waveforms. *Geophysical Research Letters*, 34(9). <https://doi.org/10.1029/2007GL029642>
- Kendall, J.-M., & Nangini, C. (1996). Lateral variations in D below the Caribbean. *Geophysical Research Letters*, 23(4), 399–402. <https://doi.org/10.1029/95GL02659>
- Ko, J. Y. T., Hung, S. H., Kuo, B.-Y., & Zhao, L. (2017). Seismic evidence for the depression of the D'' discontinuity beneath the Caribbean: Implication for slab heating from the Earth's core. *Earth and Planetary Science Letters*, 467, 128–137. <https://doi.org/10.1016/j.epsl.2017.03.032>
- Komatitsch, D., Vilotte, J. P., Tromp, J., Afanasiev, M., Bozda, E., Charles, J., & Zhu, H. (2015). *SPECFEM3D Globe v7.0.0 [software]*, Computational Infrastructure for Geodynamics.

- Konishi, K., & Borgeaud, A. F. E. (2020). *Kibrary*. [software]. <https://doi.org/10.5281/zenodo.4588195>
- Konishi, K., Fuji, N., & Deschamps, F. (2017). Elastic and anelastic structure of the lowermost mantle beneath the Western Pacific from waveform inversion. *Geophysical Journal International*, 2008, 1290–1304. <https://doi.org/10.1093/gji/ggw450>
- Konishi, K., Fuji, N., & Deschamps, F. (2020). Three-dimensional elastic and anelastic structure of the lowermost mantle beneath the Western Pacific from finite-frequency tomography. *Journal of Geophysical Research: Solid Earth*, 125(2). <https://doi.org/10.1029/2019JB018089>
- Liu, C., & Grand, S. P. (2018). Seismic attenuation in the African LLSVP estimated from PcS phases. *Earth and Planetary Science Letters*, 489, 8–16. <https://doi.org/10.1016/j.epsl.2018.02.023>
- Murakami, M., Hirose, K., Kawamura, K., Sata, N., & Yasuo, O. (2004). Post-perovskite phase transition in MgSiO₃. *Science*, 304(5672), 855–858. <https://doi.org/10.1126/science.1095932>
- Oganov, A. R., & Ono, S. (2004). Theoretical and experimental evidence for a post-perovskite phase of MgSiO₃ in Earth's D layer. *Nature*, 430(6998), 445–448. <https://doi.org/10.1038/nature02701>
- Romanowicz, B. A., & Mitchell, B. J. (2015). *Deep Earth Structure: Q of the Earth from Crust to Core* (Vol. 1, pp. 789–827). Elsevier B.V. <https://doi.org/10.1016/B978-0-444-53802-4.00021-X>
- Sun, D., Helmberger, D., Miller, M. S., & Jackson, J. M. (2016). Major disruption of D" beneath Alaska. *Journal of Geophysical Research: Solid Earth*, 121, 3534–3556. <https://doi.org/10.1002/2015JB012534>
- Suzuki, Y., Kawai, K., Geller, R. J., Tanaka, S., Siripunvaraporn, W., Boonchaisuk, S., et al. (2020). High-resolution 3-D S-velocity structure in the D" region at the western margin of the Pacific LLSVP: Evidence for small-scale plumes and paleoslabs. *Physics of the Earth and Planetary Interiors*, 307, 106544. <https://doi.org/10.1016/j.pepi.2020.106544>
- Takeuchi, N., Kawakatsu, H., Shiobara, H., Isse, T., Sugioka, H., Ito, A., & Utada, H. (2017). Determination of intrinsic attenuation in the oceanic lithosphere-asthenosphere system. *Science*, 358(6370), 1593–1596. <https://doi.org/10.1126/science.aao3508>
- Thomas, C., Kendall, J.-M., & Lowman, J. (2004). Lower-mantle seismic discontinuities and the thermal morphology of subducted slabs. *Earth and Planetary Science Letters*, 225(1–2), 105–113. <https://doi.org/10.1016/j.epsl.2004.05.038>
- Thorne, M. S., Takeuchi, N., & Shiomi, K. (2019). Melting at the edge of a slab in the deepest mantle. *Geophysical Research Letters*, 46(14), 8000–8008. <https://doi.org/10.1029/2019GL082493>
- Tsuchiya, T., Tsuchiya, J., Umamoto, K., & Wentzcovitch, R. M. (2004). Elasticity of post-perovskite MgSiO₃. *Geophysical Research Letters*, 31(14). <https://doi.org/10.1029/2004GL020278>
- Ventosa, S., & Romanowicz, B. (2015). Extraction of weak PcP phases using the slant-stacklet transform –II: Constraints on lateral variations of structure near the core-mantle boundary. *Geophysical Journal International*, 203(2), 1227–1245. <https://doi.org/10.1093/gji/ggv364>
- Whittaker, S., Thorne, M. S., Scherrer, N. C., & Miyagi, L. (2015). Seismic array constraints on the D" discontinuity beneath Central America. *Journal of Geophysical Research: Solid Earth*, 121(1), 152–169. <https://doi.org/10.1002/2015JB012392>. Received
- Woodhouse, J. H., & Wong, Y. K. (1986). Amplitude, phase and path anomalies of mantle waves. *Geophysical Journal of the Royal Astronomical Society*, 87, 753–773. <https://doi.org/10.1111/j.1365-246X.1986.tb01970.x>
- Yamaya, L., Borgeaud, A. F., Kawai, K., Geller, R. J., & Konishi, K. (2018). Effects of redetermination of source time functions on the 3-D velocity structure inferred by waveform inversion. *Physics of the Earth and Planetary Interiors*, 282, 117–143. <https://doi.org/10.1016/j.pepi.2018.04.012>
- Yu, S., Garnero, E., Shim, S. H. D., & Zhao, C. (2014). *Ultra low velocity zone existence in the high shear velocity region beneath cocos plate, Central America, and the Caribbean*. AGU. Abstract D153A-4358 presented at 2019 Fall Meeting, 15-19 Dec.